Welding-induced stresses and distortion in high-strength steel T-joints: Numerical and experimental study

Ghafouri Mehran, Ahola Antti, Ahn Joseph, Björk Timo

DOI: 10.1016/j.jcsr.2021.107088

Journal of Constructional Steel Research 189 (2022) 107088

Contents lists available at ScienceDirect

Journal of Constructional Steel Research

journal homepage: www.elsevier.com/locate/jcsr

Welding-induced stresses and distortion in high-strength steel T-joints: Numerical and experimental study

Mehran Ghafouri [a,*], Antti Ahola [a], Joseph Ahn [b], Timo Björk [a]

[a] Laboratory of Steel Structures, School of Energy Systems, LUT University, P.O. Box 20, 53851 Lappeenranta, Finland
[b] Department of Mechanical Engineering, Imperial College London, South Kensington Campus, London SW7 2AZ, UK

ARTICLE INFO

Keywords:
Welding simulation
Residual stress
Finite element simulation
High strength steel
Welding distortion

ABSTRACT

The main objective of this study is to develop a computational approach based on the finite element (FE) method to efficiently predict welding deformations and residual stresses of fillet welded T-joints made of high strength steel (HSS), S700, using different welding sequences and external constraints. With this aim, thermo-elastic-plastic FE models were developed in ABAQUS FE code based on Goldak's double ellipsoidal heat source model, material non-linearity and geometrical non-linearity. The results of the FE models in terms of temperature fields, angular distortion and transverse residual stress were verified against measurements. The results showed that angular distortion and transverse residual stress were significantly impacted by configuration of the external constraints, while longitudinal stress were less affected. It was found that the welding sequences had a smaller effect on the sequential and cumulative welding distortions and final residual stresses than the configuration of the external constraints. The results of this study are meaningful for understanding of the calibration and accuracy of FE computational approaches to simulate welding processes. Additionally, from a practical point of view, the results are important to understand the distortions and residual stress control measures of structural members made from HSSs.

1. Introduction

Gas metal arc welding (GMAW) is widely used to make permanent joints between mechanical components and structural members, primarily due to its flexibility, practicality and high productivity [1]. However, localized and rapid heating due to heat input from the welding torch to the base material followed by non-uniform cooling in the weld zone give rise to residual stresses and distortions in the weld. The formation of residual stresses and deformations, which is a significant problem in welded structures, is affected by a number of factors, which fall mainly into three categories. Design-related factors include joint type and geometrical dimensions; and material-related factors comprise temperature-dependent thermal and mechanical properties of the base material and filler material. The third category encompasses process-related factors including the welding method, welding sequences, heat input and mechanical boundary conditions [2].

Some residual stresses, mainly compressive stresses, can be beneficial. Nevertheless, most residual stresses are detrimental to the service performance and integrity of the welded structure. Tensile residual stresses in the fusion zone (FZ) and heat-affected zone (HAZ) are known to contribute to acceleration of a wide range of degradation phenomena in components and structures [3]. Reduced fatigue life of welded connections [4], decreased buckling strength [5], increased incidence of brittle fracture [6] and stress corrosion cracking [7,8] can all be attributed to residual stresses. Welding-induced distortion, another unwanted side-effect frequently found in GMAW welds, can cause undesirable secondary bending stresses, and it often results in loss of dimensional accuracy, which leads to extra costs for additional correction can cause schedule delays. Welding distortions can degrade joint quality, seriously impair fabrication and assembly of structural members, and, in extreme cases, might lead to the joint or component being unusable.

In the recent decades, HSSs have increasingly been used to reduce the weight of structures and improve their energy efficiency. The excellent strength-to weight ratio offered by HSSs may, however, be degraded when they experience HAZ softening and strength reduction from the applied welding heat input [9–11]. Fillet welds are commonly used in a wide range of steel structures such as plate girders and trusses. Structural members containing T-joints, are prone to different types of welding-induced distortions, of which angular distortion is a focus of

* Corresponding author.
E-mail address: mehran.ghafouri@lut.fi (M. Ghafouri).

https://doi.org/10.1016/j.jcsr.2021.107088
Received 17 October 2021; Received in revised form 3 December 2021; Accepted 4 December 2021
Available online 17 December 2021

this work. Assessment of residual stresses after welding can be challenging because the use of destructive methods is impossible and non-destructive methods have their own restrictions. For example, the X-ray diffraction (XRD) method for measurement of residual stresses of T-joints has some limitations as, depending on the stiffener height, the measuring head often cannot reach regions near the weld toe.

In view of the damaging consequences of welding residual stresses and deformations, it is important to accurately predict and efficiently evaluate such stresses and distortions to be able to produce robust designs and ensure the safety of welded components and structures [1,3]. Thus, it is a meaningful task to develop a reliable computational approach based mainly on the FE method to predict welding thermal fields as well as welding stresses and distortions. In the past, there have been numerous studies on FE welding simulation for different materials [12–17], different joint types [18–22] and different welding processes [3,18,23]. FE simulation of welding of T-joints has been used in a number of research studies [12,18,24,25], however, there is still a lack of data in the literature regarding the effect of different welding sequences and external constraints on the welding distortions and residual stresses of HSSs.

The objective of the current research is to develop three-dimensional sequentially coupled thermo-mechanical models in ABAQUS FE software [26] to predict welding-induced distortions and residual stresses in T-joints made of HSS S700MC PLUS under different mechanical boundary conditions and for different welding sequences. Four fillet welding cases with two welding sequences and two specific mechanical boundary conditions are considered. Thermal fields are simulated by implementation of Goldak's double ellipsoidal heat source model [27] in the user-subroutine DFLUX. Thermal loss is modeled by applying the combined effects of radiation and convection, which are implemented in the user-subroutine FILM. Nodal temperatures calculated in the thermal analysis are mapped into a mechanical model to calculate stresses and strains for each welding case. The results of the simulations with respect to temperature fields, welding-induced residual stresses before and after release from the clamps, and sequential angular deformations due to each welding pass as well as final angular distortions are verified with experimental measurements.

2. Experimental setup

2.1. Materials

The base material in this study was HSS S700MC PLUS, which is a low carbon and low alloy HSS offering a minimum yield strength of 700 MPa. This HSS is manufactured using a modern hot strip rolling method integrated with direct quenching [28]. The filler material used in the welding process is ESAB OK AristoRod 13.29 solid wire with 1 mm diameter. This filler material has practically the same strength level as the base material. The chemical compositions of the base and filler materials based on the material certificates of the manufacturers are presented in Table 1.

2.2. Specimens and welding procedure

T-joint specimens with identical geometry were manufactured from 6 mm thick hot rolled strips of S700. The dimensions of the base plate and stiffener were 460 × 130 mm and 130 × 25 mm, respectively. The convention for the welding direction was adopted in the Y-direction, while Z is normal to the top surface of the base plate. Fig. 1 shows the experimental set up for one of the specimens clamped from one side. The welding parameters presented in Table 2 were selected in order to achieve the designed leg size of 6 mm.

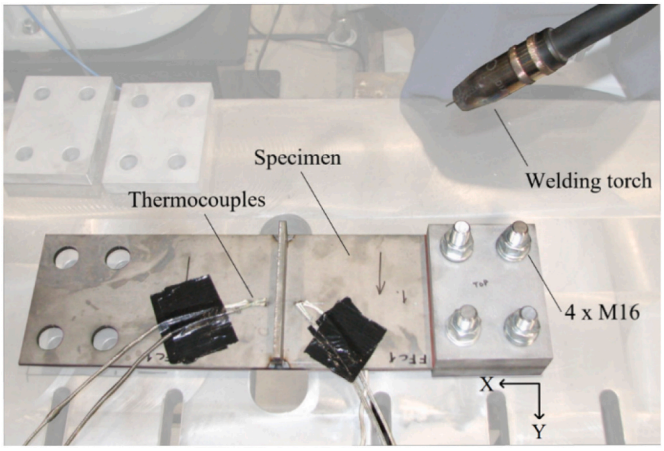

Fig. 1. Experimental set up for one of the specimens.

Based on a welding efficiency coefficient of 0.85 for GMAW [29], a net heat input value of 0.79 kJ/mm was applied to the specimens during fillet welding of the T-joints.

The fillet welding procedure consisted of deposition of filler material on both sides of the stiffener to make double-sided fillet welds. Four specimens in total were fillet welded using two welding sequences (see Fig. 2) and two different mechanical boundary conditions to consider the effects of external restraint on the residual stresses and distortions of fillet welded T-joints.

In the labelling of the specimens, the first letter shows the applied mechanical boundary conditions. **C** indicates the cases which were clamped at both ends and **F** signifies that the specimen was clamped at one end while the other end was free. **S1** and **S2** are welding sequences for fillet welding as illustrated in Fig. 2. In order to facilitate the drawing of conclusions for the different welding cases, the labels adopted for the specimens and the conditions the labels refer to are summarized in Table 3.

2.3. Temperature measurements

Temperature histories during the fillet welding were monitored using K-type thermocouples attached on the top and bottom surfaces of the specimens. For each specimen, four thermocouples (A–D) were used to record the temperature on the top surface, including the high temperature HAZ and regions with lower temperatures, to be able to verify the temperature field obtained from the corresponding FE model. For

Table 2
Welding process parameters.

Voltage (V)	Current (A)	Travel speed (mm/s)	Wire diameter (mm)	Wire feed rate (m/min)	Tip distance (mm)	Shielding gas
25	260	7	1	12.5	16	Ar + 8% CO_2

Table 1
Chemical compositions of S700MC PLUS and ESAB OK AristoRod 13.29 (wt%).

Material	C	Si	Mn	P	S	Al	Ti	Cr	Ni	Mo	Nb	V
S700 MC	0.12	0.25	2.10	0.02	0.01	0.015	0.15				0.09	0.2
AristoRod 13.29	0.089	0.53	1.54	–	–	–	–	0.26	1.23	0.24	–	–

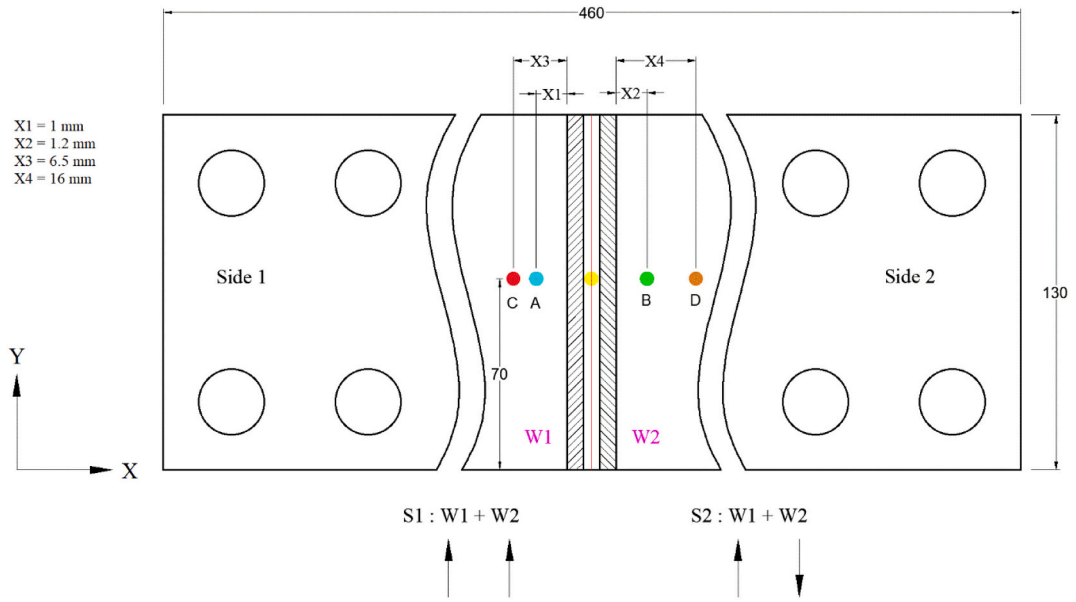

Fig. 2. Specimen configuration, positions of thermocouples and illustration of applied welding sequences. (Units in mm).

Table 3
Labels adopted for specimens in welding experiments.

Label	Condition
FS1	One **F**ree end, welding **S**equence **1**
FS2	One **F**ree end, welding **S**equence **2**
CS1	Both ends **C**lamped, welding **S**equence **1**
CS2	Both ends **C**lamped, welding **S**equence **2**

each welding case, one thermocouple was also used at the bottom side to facilitate verification of temperature distribution through the thickness of the specimen. The positions of the thermocouples are shown schematically in Fig. 2. It should be noted that the dimensions X1, X2, X3 and X4 refer to the distance between the weld toe and the thermocouples A, B, C and D, respectively. The real values were determined based on measurement data from a Hexagon 3D scanner.

3. Finite element model

From a complexity point of view, simulation of welding can become very complicated as the welding process includes coupled interactions between heat and mass transfer, material science, welding technology, microstructural evolution, computational sciences, and mechanics of materials. Capturing all the interactions involved in the welding process in a simulation is a highly demanding task and it is possible that convergence might not be reached. Thus, removing inconsequential aspects which only add complexity to a simulation and elaborating an efficient model with sufficient accuracy are of paramount importance.

In this research, evolution of stresses and strains of fillet welded specimens were studied by developing three-dimensional thermo-elastic-plastic FE models in ABAQUS FE Software. Since dimensional changes in welding are negligible and the effect of the mechanical field on the thermal field is insignificant, a sequentially coupled formulation was adopted [30]. For each case, the solution procedure consisted of two steps. In the first step, the non-linear transient temperature field was captured by solving the heat conduction equation in a thermal analysis. These nodal temperatures were later transferred and mapped into the subsequent mechanical analysis as a thermal load to find the structural response and calculate the residual stress field and nodal displacements.

3.1. FE model geometry and mesh

Modeling of the deposited filler metal was carried out based on the experimentally measured weld leg and throat sizes. In each case, in order to facilitate transfer of the nodal temperature data from the thermal model to the mechanical model, the same FE mesh structure was used with an identical number of elements but different element types, as shown in Fig. 3. An 8-node linear heat transfer brick (DC3D8) with temperature as the only degree of freedom was used in the thermal analysis and a first order 8-node reduced integration brick element (C3D8R) with hourglass control was applied in the mechanical analysis. By using reduced integration elements, shear locking is prevented and less computational time as well as better convergence is achieved [31]. Convergence studies regarding the effect of mesh density on the accuracy of the simulation results were performed in a previous study [21]. A fine mesh grid with the smallest element size of 3 × 0.5 × 1 mm was applied in the FZ and adjacent HAZ for all the models. The size of the elements increased progressively from the weld toes towards the outer edges of the specimens. A fine mesh grid with a total number of 30,738 elements was able to represent stress and strain values in the weld regions with sufficient accuracy and acceptable computation time.

3.2. Thermal analysis

In this study, a partial differential equation from Fourier's law of heat conduction and energy conservation, shown in Eq. (1), was applied to solve the transient temperature field during welding (T) in time (t) and space (x, y, z):

$$\rho(T)c_p(T)\frac{\partial T}{\partial t}=\frac{\partial}{\partial x}\left(k(T)\frac{\partial T}{\partial x}\right)+\frac{\partial}{\partial y}\left(k(T)\frac{\partial T}{\partial y}\right)+\frac{\partial}{\partial z}\left(k(T)\frac{\partial T}{\partial z}\right)+\dot{Q}_v \quad (1)$$

where T is temperature and t represents time. $\rho(T)$, $c_p(T)$ and $k(T)$ are temperature-dependent density, specific heat, and thermal conductivity, respectively. These temperature-dependent thermo-physical properties were obtained for the base material from the literature [18] and are shown in Fig. 4. It should be noted that the units are arranged so that all properties can be shown in a single graph.

As the filler material in this research shares the same matching strength configuration as the base material, the two metals were defined as identical materials and the same properties were assigned to both. $\dot{Q}_v$ (W/m3) is the volumetric heat source density or internal heat generation

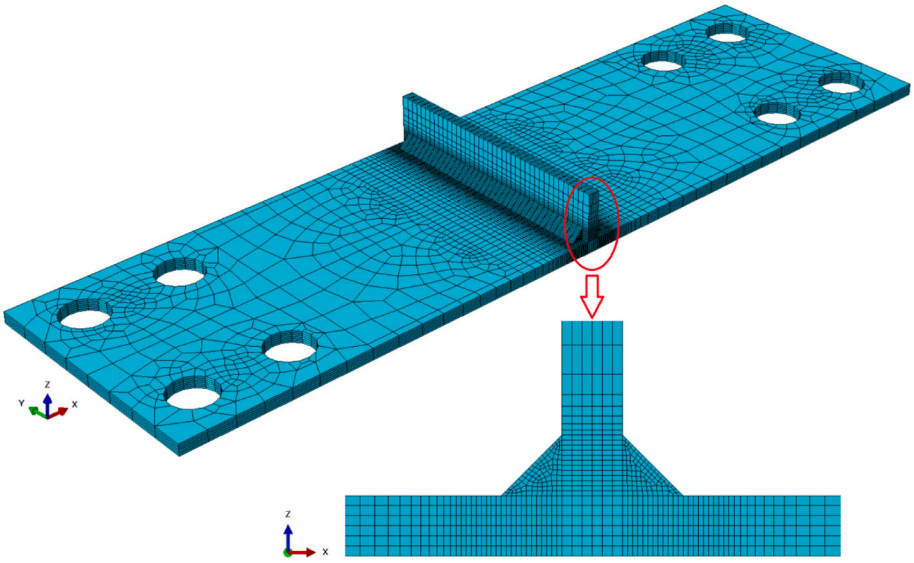

Fig. 3. Mesh details of the fillet welded T-joint.

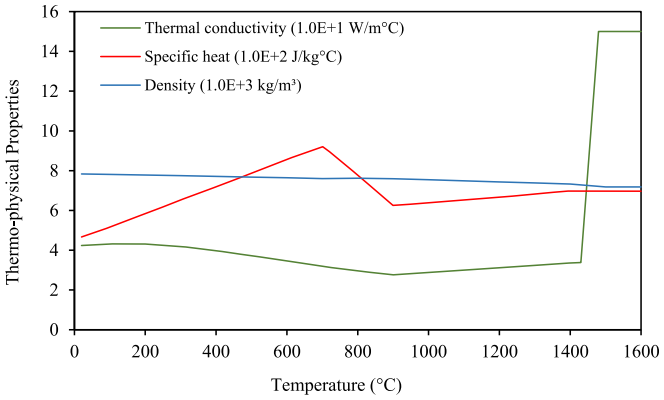

Fig. 4. Temperature-dependent thermo-physical properties of S700.

rate. Arc energy transferring from the moving heat source to the base and filler materials was modeled as a volumetric heat source with double ellipsoidal distribution proposed by Goldak et al. [27]. This model considers two heat flux distributions, one for the front half and one for the rear half of the heat source. The heat distributions are described by Eqs. (2) and (3), respectively:

$$q_f(x,y,z,t) = \frac{6\sqrt{3}f_f Q}{ab_f c\pi\sqrt{\pi}}\, e^{-3\left(\frac{x^2}{a^2}+\frac{[y-vt-y_0]^2}{b_f{}^2}+\frac{z^2}{c^2}\right)}, \quad y \geq 0 \tag{2}$$

$$q_r(x,y,z,t) = \frac{6\sqrt{3}f_r Q}{ab_r c\pi\sqrt{\pi}}\, e^{-3\left(\frac{x^2}{a^2}+\frac{[y-vt-y_0]^2}{b_r{}^2}+\frac{z^2}{c^2}\right)}, \quad y < 0 \tag{3}$$

where x, y and z are coordinates in the reference system. Q is the power of the welding arc ($Q = VI\eta$) calculated based on the welding current (I), voltage (V) and welding efficiency coefficient (η). a, b_f, b_r and c are characteristics of the weld pool, while f_f and f_r are dimensionless fractions of heat deposited in the front and rear half of the heat source, respectively. Taking the continuity of the heat source into consideration, the following relationships are observable:

$$\frac{f_r}{b_r} = \frac{f_f}{b_f} \tag{4}$$

$$f_f + f_r = 2 \tag{5}$$

Representation of the applied heat source model was accomplished using the ABAQUS user subroutine DFLUX programmed in FORTRAN. To simulate the moving heat source for fillet welding of the T-joints, two translation and rotation matrices were defined to transform points in the global coordinate system into the local coordinate system at angles of $-45°$ and $45°$ for side 1 and side 2, respectively:

$$\begin{bmatrix} x \\ y \\ z \end{bmatrix} = \begin{bmatrix} cos45 & 0 & sin45 \\ 0 & 1 & 0 \\ -sin45 & 0 & cos45 \end{bmatrix} \begin{bmatrix} X - X_0 \\ Y - Y_0 \\ Z - Z_0 \end{bmatrix} \tag{6}$$

$$\begin{bmatrix} x \\ y \\ z \end{bmatrix} = \begin{bmatrix} cos45 & 0 & -sin45 \\ 0 & 1 & 0 \\ sin45 & 0 & cos45 \end{bmatrix} \begin{bmatrix} X - X_0 \\ Y - Y_0 \\ Z - Z_0 \end{bmatrix} \tag{7}$$

where x, y and z are nodal coordinates in the local coordinate system and X, Y and Z are nodal coordinates in the global coordinate system. The position of the heat source was calculated with respect to time, nodal coordinates, and welding speed in the subroutine DFLUX. At each integration point, non-uniform flux distribution was then calculated by DFLUX as a function of time, the coordinates of the heat source, and using the power of the welding arc. In order to predict welding residual stresses and distortions, the temperature field must be determined accurately, which necessitates calibration of the heat source model. Calibration of the heat source was performed by adjusting the heat source parameters in such a way that a close agreement was reached between the nodal temperatures captured by the thermocouples in the experimental measurements and the corresponding nodal temperatures obtained from the simulation. Further calibration was done by matching the boundaries of the FZ and HAZ from the FE model against the macrograph of the weld cross section. The heat source parameters and their values adjusted to perform thermal analysis are summarized in Table 4.

Table 4
Adjusted heat source parameters.

Parameter	a (mm)	b_f (mm)	b_r (mm)	c (mm)	f_f	f_r
Value	7	4	10	10	0.57	1.43

Ambient as well as initial temperatures for all simulation cases were set to 20 °C. In terms of capturing the temperature field during welding, a unique solution will be reached when Eq. (1) is solved subject to specific boundary conditions. Thermal boundary conditions are generally applied in welding simulations to model the heat loss due to convection and radiation from free surfaces of the welded specimen, as shown schematically in Fig. 5. The distance between the clamps and heat source is large enough that temperature does not rise at the clamping areas, and, heat transfer between the base plate and clamps by means of conduction was hence ignored. The specimens are assumed to experience heat loss by means of convection and radiation. Heat loss during welding is generally modeled based on Newton's law of cooling and Stefan-Boltzmann's law to account for heat transfer due to convection and radiation, respectively. An alternative method in terms of heat loss during welding is to consider the combined effect of convection and radiation. In this study, the matter was addressed by defining a temperature-dependent heat transfer coefficient expressed in the form of two mathematical expressions as practiced by other researchers [32,33] and shown by Eq. (8):

$$h = \begin{cases} 0.0668 \times T \left(\dfrac{W}{m^{2\circ}C}\right) & 0 \le T \le 500 \\ 0.231 \times T - 82.1 \left(\dfrac{W}{m^{2\circ}C}\right) & T \ge 500 \end{cases} \quad (8)$$

where T (°C) is temperature and h denotes the temperature-dependent heat transfer coefficient. These mathematical expressions were implemented in the user subroutine FILM to model the combined thermal boundary conditions.

The coupled problem between the solid and liquid phases is not included in the ABAQUS package, and directly, modeling the fluid flow in the weld pool is thus not possible in such FE software. Fluid flow in the weld pool is, however, very important and has a significant effect on the temperature distribution in the weld pool. Artificially increased thermal conductivity was applied to account for the effect of fluid flow in the FZ. For temperatures higher than the liquidus temperature, thermal conductivity was considered to be four times as large as the value at room temperature, and increases linearly between the solidus and liquidus temperatures. The latent heat of fusion was considered to account for the thermal effects of solidification in the weld pool. The assumed value for latent heat was 270 × 10^3 J/kg between the solidus temperature of 1430 °C and liquidus temperature of 1480 °C.

3.3. Mechanical analysis

Nodal temperatures computed for each time increment in the thermal analysis were transferred as a thermal load through predefined fields in the subsequent mechanical analysis. The structural response of the model was then calculated as the sum of individual strain rate components as expressed in Eq. (9):

$$\dot{\varepsilon}^{total} = \dot{\varepsilon}^{e} + \dot{\varepsilon}^{p} + \dot{\varepsilon}^{th} \quad (9)$$

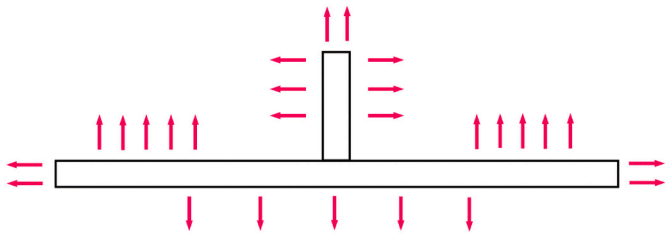

Fig. 5. Illustration of heat loss (convection and radiation) or thermal boundary conditions applied to the T-joints.

where $\dot{\varepsilon}^{total}$ is total strain rate. $\dot{\varepsilon}^{e}$, $\dot{\varepsilon}^{p}$ and $\dot{\varepsilon}^{th}$, correspond, respectively, to elastic, plastic, and thermal strain increments. It should be noted that the strain rate component due to phase change was not considered in this study and the strain rate component due to creep was also neglected since the time period at high temperature was limited to a few seconds throughout the entire thermal cycle. Elastic strain was calculated using isotropic Hooke's law with temperature-dependent Young's modulus and Poisson's ratio. A rate-independent plastic model with temperature-dependent mechanical properties, isotropic hardening law and the Von Mises yield criterion were used to model the plastic behavior of the material. Thermal strain was calculated using a temperature-dependent thermal expansion coefficient. The required mechanical properties of the base and filler metals in the structural analysis, namely, temperature-dependent yield strength, Young's modulus, Poisson's ratio and the thermal expansion coefficient were taken from literature [18] and are shown in Fig. 6.

An annealing step was modeled by defining an annealing temperature. When the temperature of a material point exceeds the annealing temperature, strain hardening memory is annihilated by resetting the equivalent plastic strain to zero. Provided that the temperature of that material point falls below the annealing temperature during cooling, regeneration of work hardening happens if the material deforms plastically [12,19]. The annealing temperature was set to 900 °C in this study. In order to avoid convergence problems, the values of yield strength and Young's modulus were not considered to be zero for molten material, but they were reduced to 5 MPa and 5 GPa, respectively.

Prescription of external constraints is a common method to reduce welding deformations. This important task is, however, problematic since the application of mechanical constraints affects the residual stress field and welding distortions. Greater constraints give rise to a residual stress field and reduces welding deformations by increasing plastic strains and decreasing elastic strains, which are responsible for distortions after removing clamps. This implies that in an over-constraint situation, residual stresses might accumulate and result in welding-induced cracks, while deformations derived from an under-constraint situation might lead to dimensional instability, and, design of the welding fixtures must thus be done meticulously [12]. Two different clamping configurations were applied in the experiments and corresponding mechanical boundary conditions were considered in the FE models, as shown in Fig. 7. This approach makes it possible to analyze the development of residual stresses and distortions due to different mechanical boundary conditions and to optimize production procedures with the aim of obtaining smaller levels of distortions and welding residual stresses. One clamping set up was applied in which the related specimen was fixed rigidly at one end in a specified area, while the other end was free to experience angular distortion. Mechanical boundary conditions in the related FE model were set so that all the nodes in that area were restricted rotationally and translationally, as shown in Fig. 7 (a). The other clamping condition was set to rigidly fix both ends of the

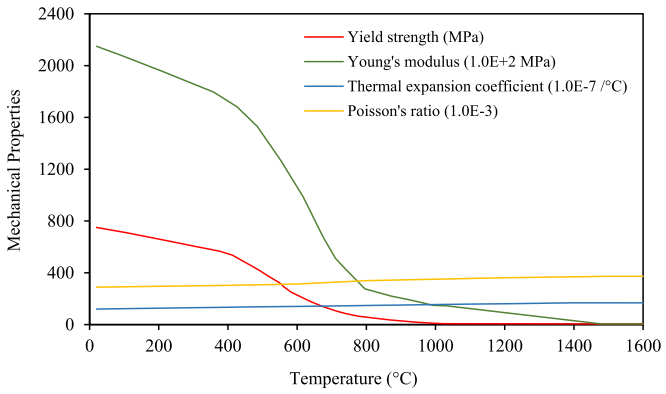

Fig. 6. Temperature-dependent mechanical properties of S700.

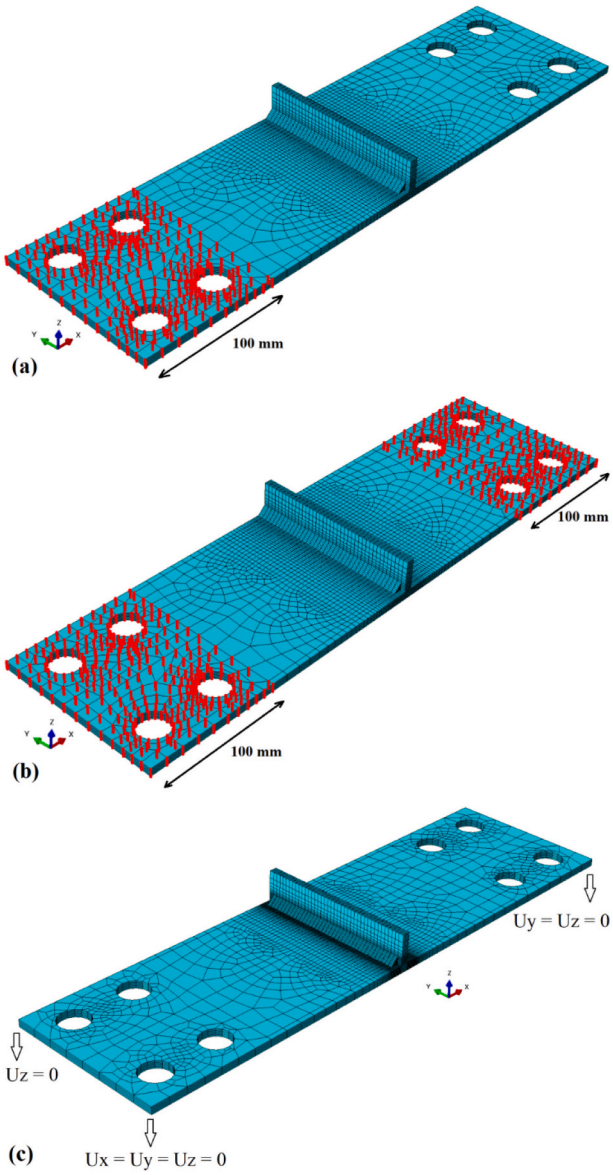

Fig. 7. Representation of different mechanical boundary conditions assigned to the FE models for mechanical analyses: (a) one end fixed and the other end free; (b) both ends fixed; and (c) after removal of the clamps.

related specimen in specified areas. As shown in Fig. 7(b), in the corresponding FE model, the boundary conditions were considered to prevent rotation and translation of all the nodes in the determined areas. After welding and reaching the ambient temperature, in all the cases, the mechanical boundary conditions corresponding to the removal of the clamps were set to prevent the rigid body motion, as shown in Fig. 7(c).

Modeling of the gradual deposition of filler material was performed, which is named element birth and death technique (model change) in ABAQUS [34]. In this modeling method, elements corresponding to the weld metal initially have inactivated status. As soon as the welding torch approaches and the filler material melts, the status of the heated element is changed from inactivated to reactivated and the specified temperature-dependent material properties are assigned.

4. Results and discussion

4.1. Results of thermal analysis

Obtaining accurate calculated welding-induced stresses and distortions, necessitates accurate prediction of the welding temperature field. The temperature distribution obtained from FE simulation at halfway during welding of the S700 T-joint specimen SF2 is shown in Fig. 8. The FE model consisted of 2 regions of very fine mesh around the heat source in the FZ and HAZ where the temperature gradient is steep at both sides of the T-joint.

Correct prediction of weld pool geometry is an indicator of accurate temperature distribution in the FZ and HAZ. Calibration of welding temperature histories necessitates prediction of the shape and size of the weld pool and matching of the simulated weld pool geometry to the experimental macrograph obtained from the polished and etched weld cross section. The region of simulated molten metal or FZ, depicted in Fig. 8 in light gray, was determined based on the temperature contour above the liquidus temperature (1480 °C).

The cross section of the fillet weld at the mid-section of the specimen, which shows the depth of penetration, is compared with the simulation in Fig. 9(a). The dimensions of the FZ, i.e., the width and length of the weld pool at the end of the welding path, are compared with the simulation in Fig. 9(b).

As shown in Fig. 9(a) and (b), the FZ boundaries and finger-like penetration as well as the dimensions of the weld pool are well-captured by the simulation, which is a result of the realistic temperature distribution and correct calibration of the heat source model. However, small reinforcement, was not modeled as it was assumed to have a negligible effect on development of residual stresses and welding distortions [12].

Close agreement between the nodal temperatures recorded by the thermocouples and the corresponding nodal temperatures from the FE simulation is the main index of correct temperature distribution and welding thermal cycles [17]. Since the welding parameters and, consequently, heat input for all the cases are similar, only one of the cases (FS2) is used for comparison in terms of welding temperature distribution. However, all the cases were calibrated and verified against experimental measurements in the same manner. The results of the thermal analysis for the welding case FS2 for passes 1 and 2 are shown in Fig. 10(a) and (b), respectively.

Fig. 10(a) compares time-temperature curves at different distances from the weld toe for the first welding pass versus numerically calculated temperature histories calibrated using thermocouple measurements. Fig. 10(b), in the same manner, shows the experimental and numerical temperature histories for the second welding pass. It can be seen in Fig. 10(a) and (b) that the second pass was started almost 5550 s after beginning of the first pass, when the specimen reached ambient temperature. In Fig. 10(a) and (b), T1–T5 are thermocouples attached at various positions on both the top and bottom side of the T-joint specimen (FS2). X1–X4, are approximate distances from the weld toe (defined in Fig. 2), which were measured post welding with the Hexagon 3D scanner, and corresponding nodal distances from the weld toe in the FE model. A good agreement between the simulated temperature field and experimentally measured thermal histories in terms of heating rate, peak temperature and cooling rate is observable. Such agreement implies that calibration of the heat source parameters (Goldak's parameters) and thermal boundary conditions was performed correctly. Thus, the FE thermal model verified by means of thermocouples and FZ boundary matching, can be considered accurate enough for nodal mapping and data transfer to subsequent mechanical analyses.

4.2. Results of simulated residual stresses and deformations

The effect of the welding sequence and mechanical boundary conditions on inhomogeneous stresses and distortions was investigated. Non-uniform heating and cooling during welding and subsequent expansion and contraction induce considerable tensile and compressive residual stresses in the weld region and adjacent HAZ. Variation in the distributions and magnitudes of the residual stresses and angular distortions due to change in the welding sequence and mechanical

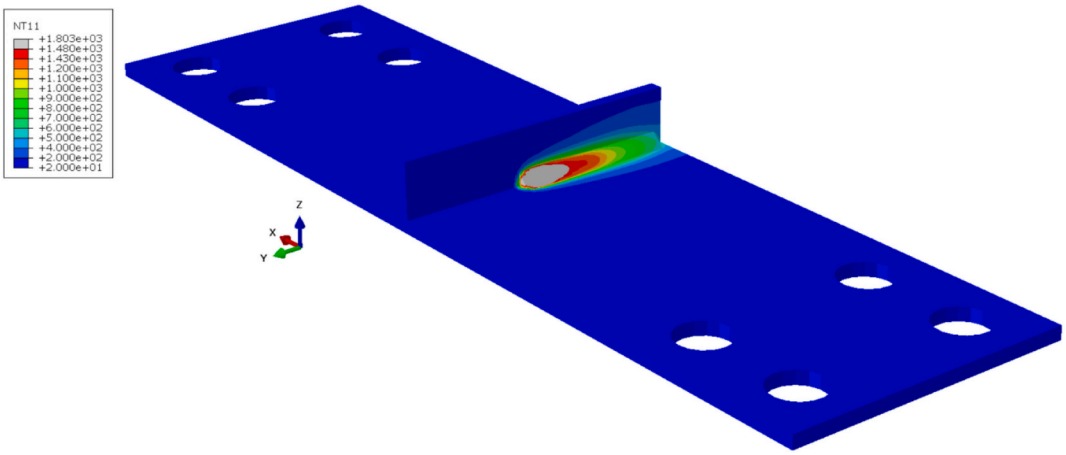

Fig. 8. Thermal contours obtained from thermal analysis of double-sided fillet welded S700 T-joint during welding.

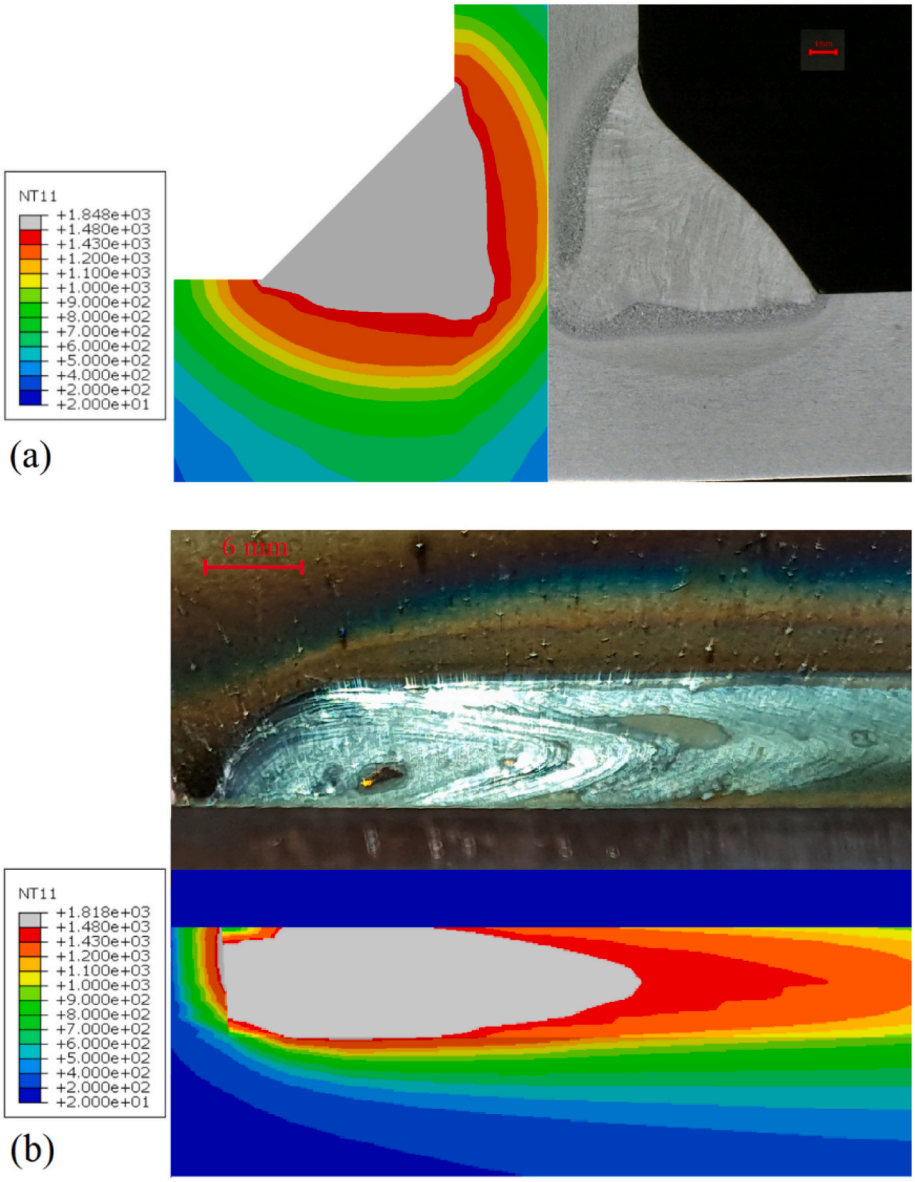

Fig. 9. Welding temperatures (NT11) and boundaries of the FZ from the experiment versus simulation: (a) through thickness; and (b) on the top surface of the specimen.

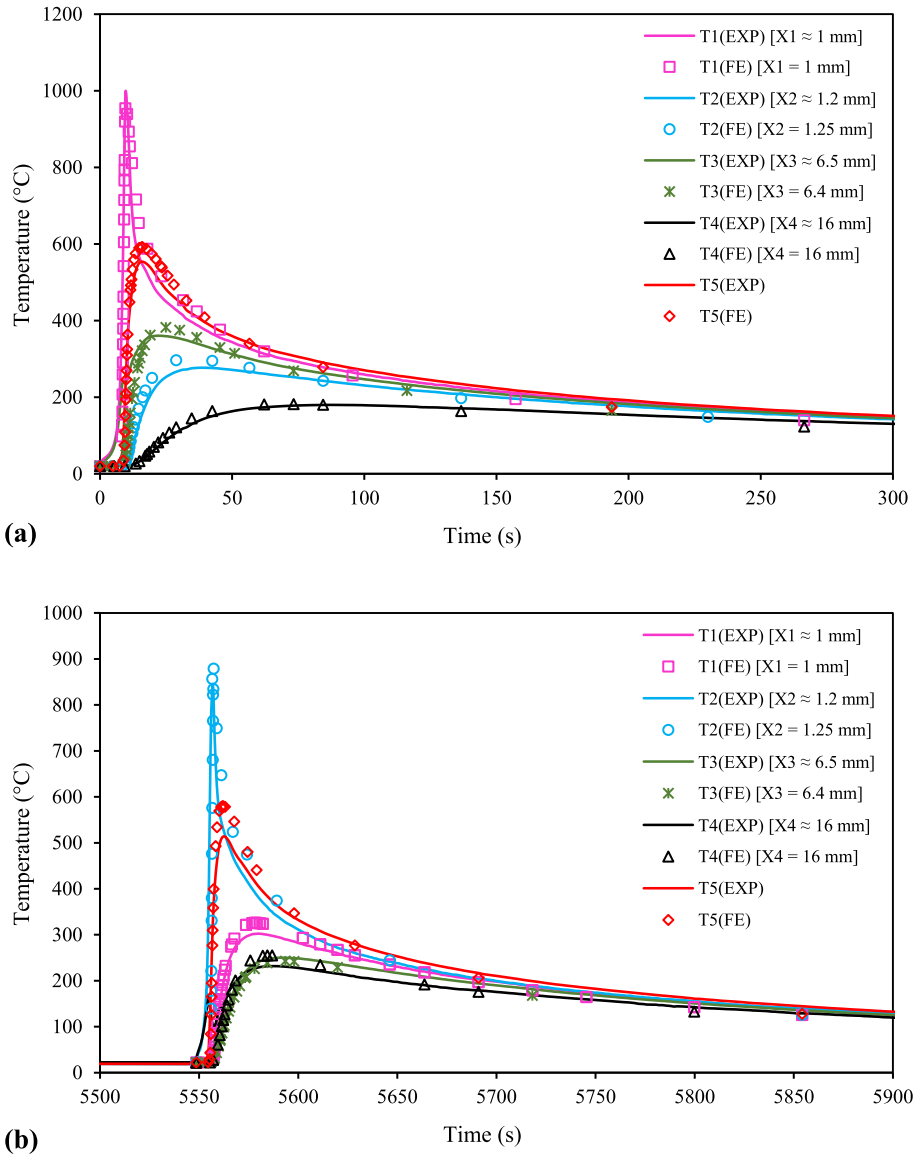

Fig. 10. Simulated temperature field versus experimentally measured temperature histories at various distances from the weld toe (Specimen FS2): (a) for the first welding pass; and (b) for the second welding pass.

boundary conditions were examined and compared with experimental measurements. It should be noted that transverse residual stresses were measured experimentally and compared with the simulation results in order to calibrate the FE models. The analysis of longitudinal stresses was performed numerically based on the validated FE model for each case. In this regard, after thermal analyses and calibration of the FE thermal models, two mechanical boundary conditions corresponding to the utilized clamping configurations were applied in the mechanical analyses. In order to verify the results of the structural analyses, measurements were performed of residual stresses and distortions. For all

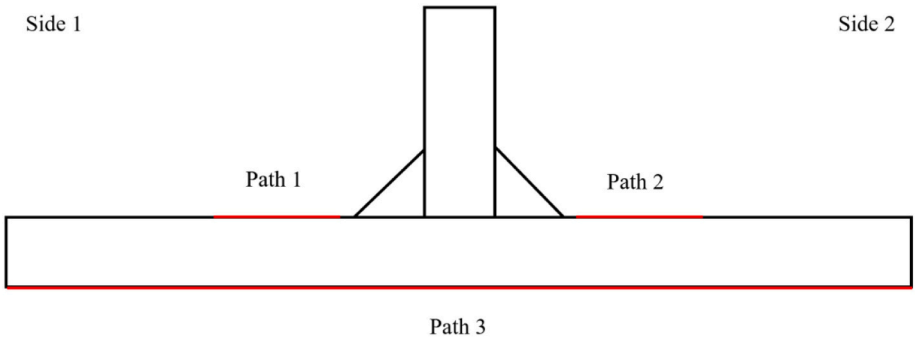

Fig. 11. Measurement paths for angular distortions and transverse residual stresses.

cases, the specimen was scanned for possible preliminary deformations prior to welding using a Hexagon ROMER Absolute Arm (resolution up to 63 μm) 3D Scanner. After each welding pass, after reaching the ambient temperature and after being released from the fixtures (specific to specimens CS1 & CS2), the specimen was scanned to be able to evaluate the sequential and cumulative angular distortions. The path in the mid-section of the specimens in the transverse direction (Path 3) along which angular distortions are measured at the bottom side of the specimens, is shown schematically in Fig. 11.

Transverse residual stresses on the top surface of the T-fillet specimens along the two specified paths (see Fig. 11) in the mid-section (Path 1 and Path 2) were measured using XRD by a Stresstech X3000 G3 device with a collimator diameter of 1 mm. It should be mentioned that for specimens CS1 and CS2, the stresses were also measured after completion of welding, but prior to release from the fixtures, in addition to measurement of the residual stresses after release from the fixtures.

4.2.1. Angular distortion

The contours of final angular deformations for cases FS1 and FS2 are shown in Fig. 12(a) and (b), respectively. It can be seen that the patterns of angular distortion (U3) in the *Z*-direction for welding cases FS1 and FS2 with different welding sequences and the same mechanical boundary conditions are similar, albeit with a small difference in the magnitude of the maximum deformation. It should be noted that angular distortion through thickness does not change and the same pattern of deformation thus exists at the bottom side of each specimen. Figs. 13 and 14 depict contours of angular distortion for specimens CS1 and CS2, respectively. As is shown in Figs. 13(a) and 14(a), rigid clamping at both ends of the specimens results in very small angular distortion of less than 1 mm, which happens in the mid-length of the specimens in the transverse direction. After removing these constraints, as shown in Figs. 13(b) and 14(b), final angular distortions for both specimens amounts to less than 4 mm for each end. While the difference between the magnitudes of the final angular distortions caused by using the two different welding sequences is small (comparing FS1 and FS2 as well as CS1 and CS2), the utilized external constraints result in a considerable difference between the developed angular distortions (comparing FS1 and CS1 as well as FS2 and CS2).

In order to evaluate the accuracy of the developed FE model, simulation results in terms of welding-induced angular distortions were compared with experimental measurements for all the cases. In Fig. 15 (a–d), simulated deflections (displacements in the *Z*-direction) along the transverse direction after cooling of each welding pass are plotted with solid lines for cases FS1, FS2, CS1 and CS2, respectively, while the experimental measurement data are shown with circular marks.

As is observable in Fig. 15(a) and (b), the FE models can predict welding distortions with reasonable accuracy for all the cases. For FS1 and FS2, percent errors calculated at the positions of maximum deflection after welding pass 2 are 9.3% and 10.9%, respectively. It can be seen in Fig. 15(a) and (b), that the angular distortions due to the chosen welding sequences remain very close and the maximum angular distortion produced in FS1 is only some fractions of a millimeter greater than FS2. This difference is 0.5 mm and 0.7 mm for the simulation and measurements, respectively. This implies that for T-joints which require 2 welding passes (one pass per side), adopting the opposite directions for the welding passes (on condition that one end of the specimen is free to deform) lead to smaller angular distortions compared to welding passes applied in the same direction. Although such difference compared to the size of specimens used in this study is negligible, in real applications and for structural members with larger dimensions, adopting S2 in contrast to S1 can result in considerably smaller deformation when the absolute magnitude of distortion is taken into account. With respect to the sequential angular distortions from the first and second welding passes, in both FS1 and FS2, the second welding pass produces greater deformation compared to the first pass. That is, based on the numerical results for FS1, pass 1 and pass 2, respectively, produce angular distortions of 6.57 and 7.43 mm, in which case the angular deformation due to the second pass is 13% greater than that of the first pass. For FS2, in the same vein, the angular distortions from the first and second welding passes are 6.56 and 6.94 mm, which shows pass 2 makes a greater contribution to total angular distortion (5.8% greater than pass 1). It should be noted that since the unrestrained ends deform freely in FS1 and FS2, the magnitudes and distributions of angular distortion, before and after release from the clamps remain unchanged. Thus, it was decided to show the angular distortion results for the condition in which the specimens are cooled down to the ambient temperature while still in the clamps.

With CS1 and CS2, shown in Fig. 15(c) and (d), the difference

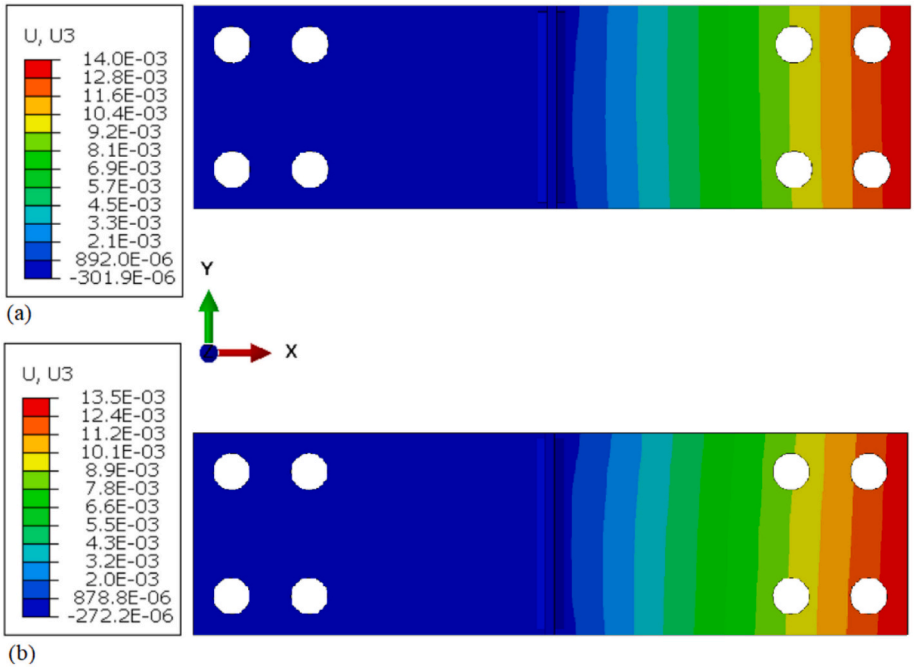

Fig. 12. Angular deformation distribution for: (a) FS1; and (b) FS2.

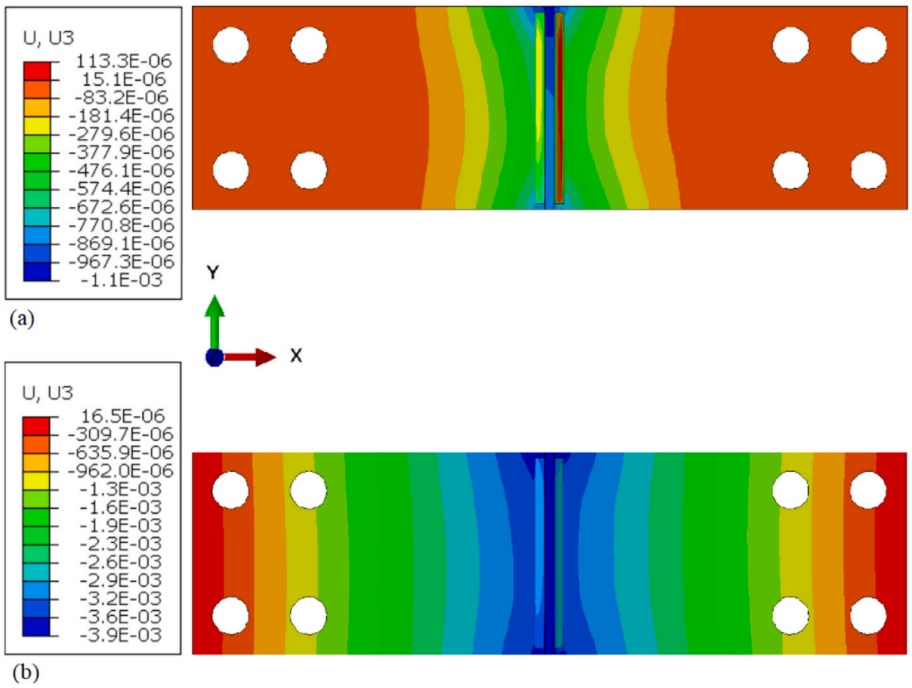

Fig. 13. Angular deformation distribution for specimen CS1: (a) after cooling and before removing the clamps; and (b) after releasing the clamps at both ends.

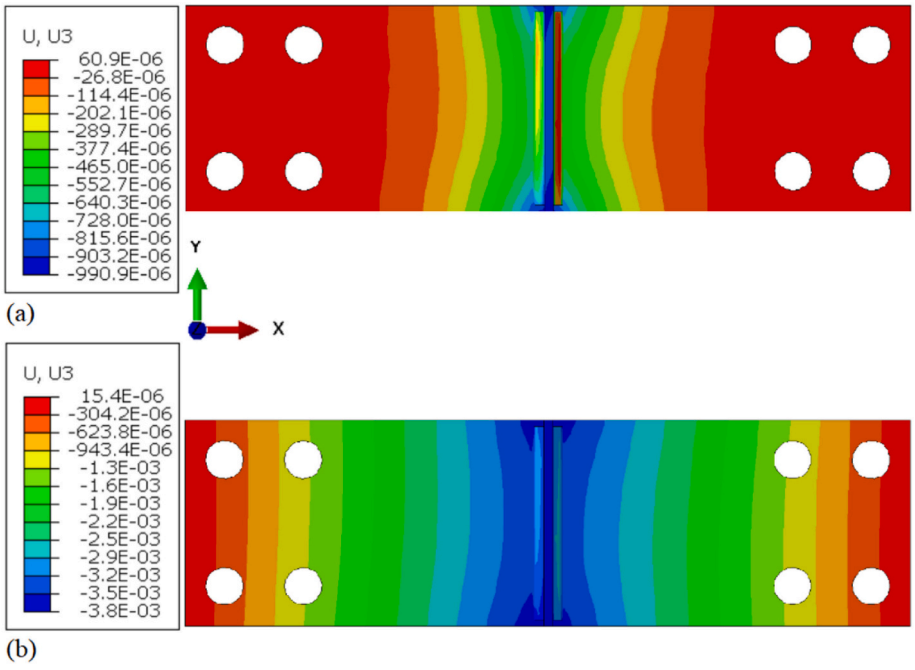

Fig. 14. Angular deformation distribution for specimen CS2: (a) after cooling and before removing the clamps; and (b) after releasing the clamps at both ends.

between the final angular distortions from the welding sequences is minor. As CS1 and CS2 are rigidly clamped at both ends, small deformations can be expected as they are in related fixtures. It should be noted that deformation data from simulations related to CS1 and CS2 were moved along the vertical axis (minimum deformation was set to zero) to be able to compare the simulation data with the measured data. The measured maximum angular distortion after cooling of the second welding pass before release from the welding fixture is almost 0.75 mm and the simulated distortion is 0.84 mm, which gives a maximum percent error of 10.7%. As can be seen from the experimental data, although the distortion dimensions are in fractions of a millimeter, welding pass 1 produces greater angular distortion than welding pass 2, as is well predicted by the simulation. The size of the maximum simulated sequential angular distortions in CS1 and CS2 are approximately 0.7 mm and 0.14 mm for pass 1 and pass 2, respectively. Although these magnitudes are small, this issue can be very important in practical applications, such as construction of plate girders, when both ends are rigidly clamped, and the dimension of the specimen is large in the transverse direction. The sequential angular distortions can also be compensated by pre-alignment of the welded plate components. After

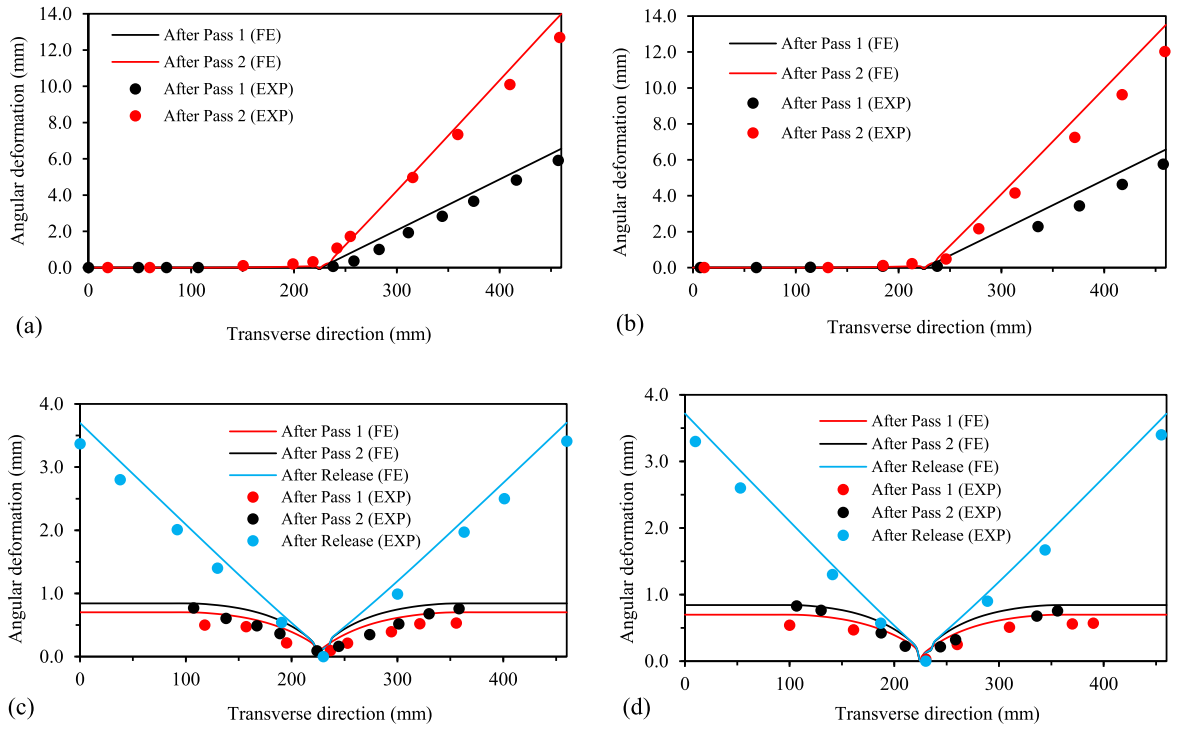

Fig. 15. Comparison of angular distortions between simulations and measurements for: (a) FS1, (b) FS2, (c) CS1, and (d) CS2 specimens.

release from the clamps, CS1 and CS2 experience angular distortion from the release of the residual stresses. The simulation results for angular distortions of CS1 and CS2 after release from the clamps are in good agreement with the measurement data. The percent error is approximately 8.4% for both cases. Total angular distortion after release experienced by specimens rigidly clamped at both ends is considerably smaller than that experienced by specimens rigidly clamped at one end. With respect to angular distortion, a comparison between FS1 and CS1, for example, shows that while FS1 experiences a total angular distortion of 14 mm (fixing one end and measuring the distortion at the other end), CS1 undergoes a total angular distortion of 7.2 mm (summation of the distortions at both ends, which is 3.5 + 3.7 mm (see Fig. 15(c)). This indicates that for the selected welding parameters and specimen size, the magnitude of the final angular distortion for the specimens clamped at one end is approximately twice as large as that for the specimens clamped at both ends. Comparison of the simulation results and measurement data shows the accuracy of the computational approach in capturing the mode and magnitude of the angular distortion.

4.2.2. *Transverse residual stresses*

Simulated transverse residual stresses (S11) versus measurements for FS1, FS2, CS1, and CS2 along the 2 specified paths (see Fig. 11) are shown in Figs. 16, 17, 18, and 19, respectively. It should be noted that path 1 and path 2 on the top surfaces start at 1 mm from the weld toes and are extended towards the outer edges of the specimens (almost 25 mm in length) and zero on the X-axis is thus at the weld toe in the relevant graphs. Simulated and measured data for path 1 and path 2 are shown in the negative and positive directions of the X-axis, respectively, based on the conventions chosen for the coordinate system. As seen in Figs. 16 and 17, both welding cases experience a similar pattern of transverse residual stress distribution along the specified paths. In both cases, the magnitude of the tensile residual stresses increases and reaches an approximate peak of 241 MPa and 189 MPa for FS1 and FS2, respectively, in the HAZ at a distance of 3–4 mm from the weld toe. Moving through the HAZ, tensile residual stresses start to fall in magnitude. With regard to evaluating the accuracy of the developed FE models, it can be seen that the simulation predictions in terms of general trend as well as magnitude of the maximum tensile residual stress are in good agreement with the XRD measurements. It should be noted that

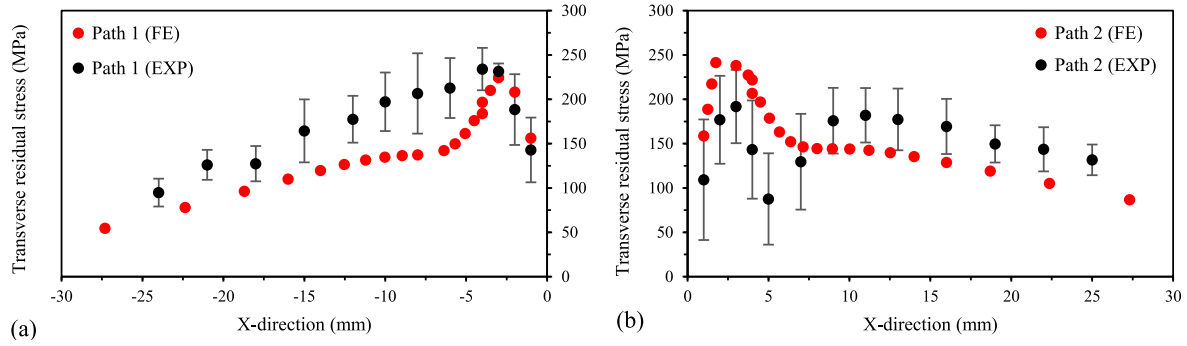

Fig. 16. Comparison of the simulated transverse residual stresses (S11) and measurements for FS1: (a) along path 1; and (b) along path 2.

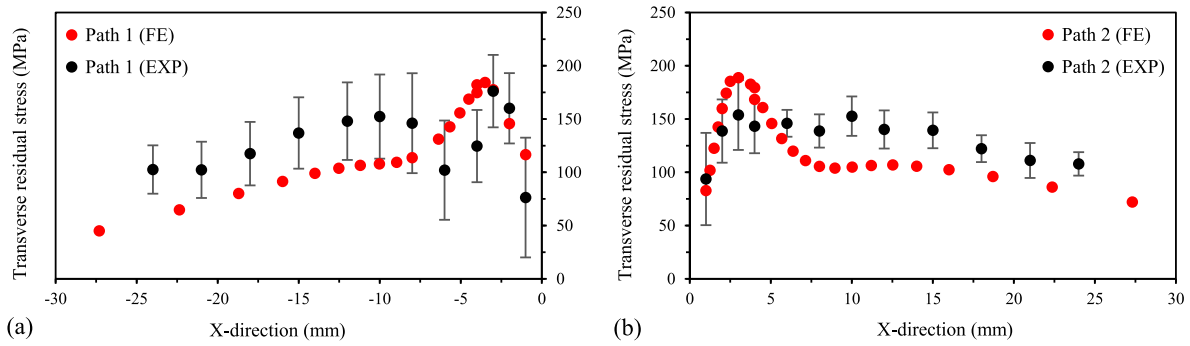

Fig. 17. Comparison of the simulated transverse residual stresses (S11) and measurements for FS2: (a) along path 1; and (b) along path 2.

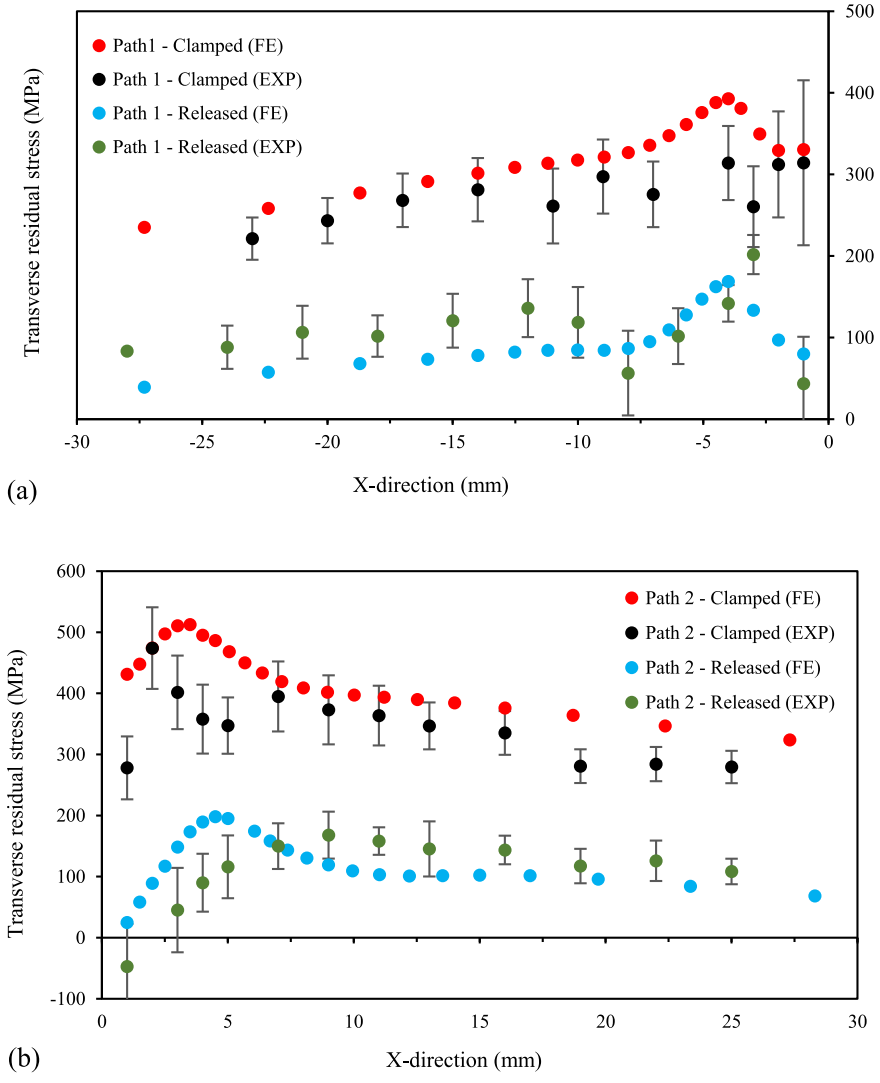

Fig. 18. Comparison of the simulated transverse residual stresses (S11) and measurements for CS1: (a) along path 1; and (b) along path 2.

XRD measurement data always falls within an error band, which should be taken into consideration when comparing FE results with experimental measurements. When comparing the simulation values and measurements for FS1, the maximum transverse tensile residual stresses predicted along path 1 and path 2 are 241 MPa and 224 MPa, in contrast to 231 ± 24 MPa and 192 ± 41 MPa from XRD measurements. In the same vein for FS2, at the position of maximum tensile residual stress along path 1 and path 2, predictions are 174 MPa and 189 MPa, respectively, whereas the measured values are 176 ± 34 MPa and 153 ± 25 MPa. The maximum tensile residual stress calculated for FS1 is 52 MPa larger than that of FS2. For mechanical boundary conditions with one end rigidly clamped, the maximum transverse tensile residual stress

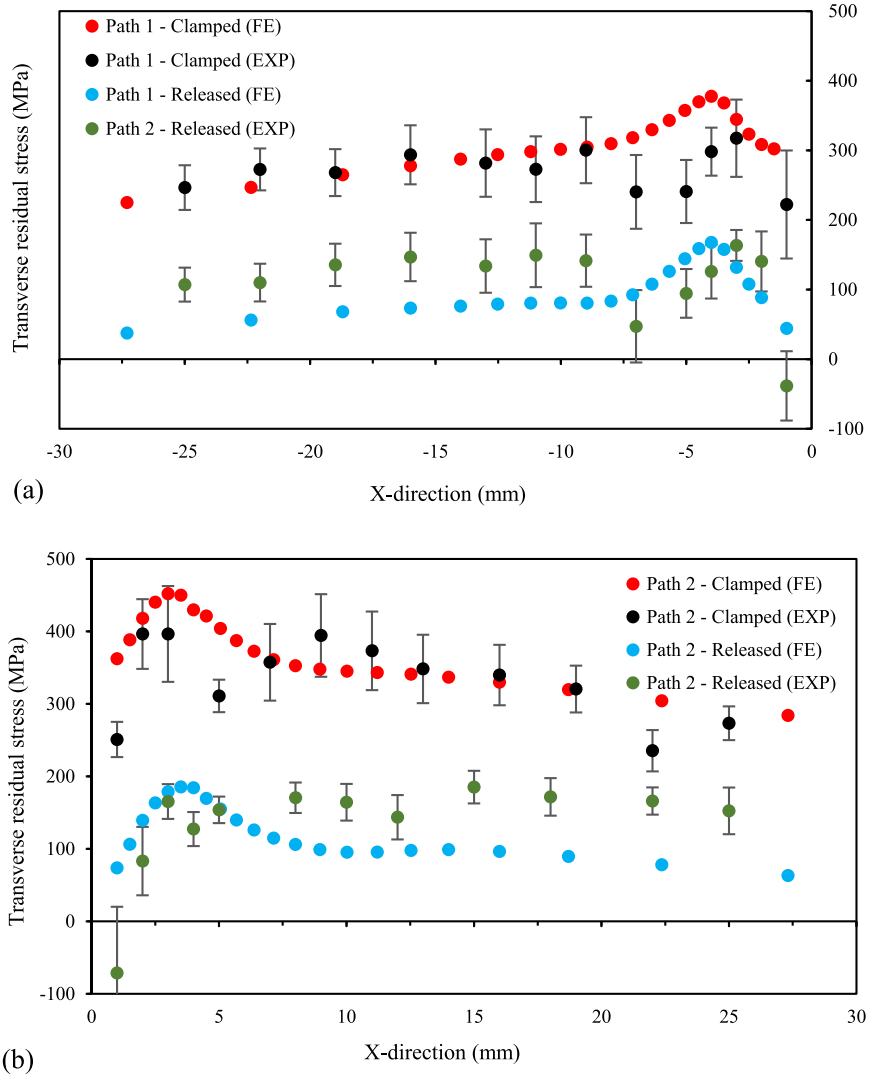

Fig. 19. Comparison of the simulated transverse residual stresses (S11) and measurements for CS2: (a) along path 1; and (b) along path 2.

reaches approximately 30% of the yield strength of the base material.

For CS1 and CS2, transverse residual stresses after welding and reaching ambient temperature while the specimens were still clamped, and residual stresses after removing the clamps are compared with corresponding data obtained from the experimental measurements. Fig. 18 compares the simulated transverse residual stresses distributions along path 1 and path 2 with measurement data for CS1. As is observable, the simulation results for CS1 are in acceptable agreement with the measurement data. As would be expected, the presence of rigid clamping with a higher degree of geometrical constraint (i.e., clamping at both ends of the specimen) prevents angular distortion to a large extent while giving rise to residual stresses. The pattern of simulated stress distribution along the two paths, before and after removing the welding fixtures, are similar, although with considerably different magnitude in the near-weld regions. That is, while the specimen is rigidly clamped, moving from the weld toe, the magnitude of the tensile residual stresses increases and reaches a peak stress of 393 MPa and 512 MPa for path 1 and path 2, respectively, at a distance of 3–4 mm from the weld toe. The high value of 512 MPa for tensile residual stress is almost 68% of the yield strength of the base material. Measurement data at the same position of maximum tensile residual stress along path 1 and 2 are 314 ± 49 MPa and 401 ± 67 MPa, respectively. Moving further towards the outer edges, tensile stresses gradually ease and fall in magnitude. The patterns of the transverse residual stresses for the specimen after removing the clamps are similar to the situation before release from the constraints, however at very different levels. The calculated peak tensile residual stress along path 2 for the released specimen is 198 MPa, which is almost 39% of the peak stress calculated along the same measurement path for the specimen with strict geometrical constraints. The situation for CS2 (see Fig. 19) is very similar to that of CS1 with slight differences in the magnitude of the peak tensile stresses in the clamped condition, which are 378 MPa and 452 MPa calculated along path1 and path 2, respectively. After removing the constraints, the transverse residual stresses in the near-weld regions of CS1 and CS2 become close and comparable to those of FS1 and FS2, although slightly greater values obtained for FS1 and FS2. The maximum tensile transverse stresses calculated for CS1 are 60 MPa and 12 MPa larger than those of CS2, for the clamped and unclamped conditions, respectively.

In all the cases, comparison of the calculated peak tensile residual stresses, indicates that the magnitude of the tensile residual stresses developed on side 1 are smaller than those of side 2 (comparing Figs. 16(a), 17(a), 18(a) and 19(a) to 16(b), 17(b), 18(b) and 19(b), respectively). These differences are smaller in the case of FS1 and FS2 than for CS1 and CS2.

4.2.3. Longitudinal residual stresses

In the current study, comparison of the longitudinal residual stresses (S22) was performed numerically based on the validated FE models for each welding case. Fig. 20 shows the longitudinal stresses calculated for FS1 and FS2 along path 1 and path 2. The curves related to FS1 are shown with solid lines and those for FS2 are plotted with dashed lines. As can be seen in the figure, for the specimens clamped at one end, the patterns and magnitudes of longitudinal stresses remain unchanged when the welding sequence is changed from S1 to S2. The pattern of longitudinal stresses are similar along both paths, however, with totally different peak tensile and compressive stresses. That is, near the weld toe, longitudinal stresses are in tensile mode for both paths, with peak stresses of approximately 380 MPa and 770 MPa for path 1 and path 2, respectively. Thermal effects may be a possible reason for this phenomenon. That is, the heat of pass 2, may modify and reduce the residual stresses developed on the weld area and HAZ of side 1 by redistribution of stresses. A similar phenomenon has been reported elsewhere [12]. Moving from the weld toe towards the outer edges, peak compressive stresses of 395 MPa and 266 MPa are found for path 1 and path 2 at approximately 7 mm from the weld toe, respectively.

Comparisons between the state of the longitudinal residual stresses before and after release from the external restraints for CS1 and CS2 are shown in Fig. 21(a) and (b), respectively. For the specimens clamped at both ends, changing the welding sequence from S1 to S2 had negligible effect on the state of the longitudinal stresses. With respect to the state of the longitudinal stresses before and after release, as can be seen in Fig. 21(a) and (b), the pattern of longitudinal stresses before and after release from the constraints remains almost identical in both cases, with, however, a shift towards the compressive side for the unclamped condition. That is, for the cases clamped at both ends, removal of the clamps had only a slight effect on the magnitudes of the tensile and compressive longitudinal stresses. The effect of unclamping is greater on transverse stresses than on longitudinal stresses for the cases clamped at both ends. The peak tensile and compressive longitudinal stresses for CS1 and CS2 are smaller in both the clamped and unclamped conditions than for FS1 and FS2. The peak tensile longitudinal stress for CS1 and CS2 is considerably smaller along path 1 than path 2, which is similar to the cases clamped at one end.

In order to investigate the sensitivity of transverse and longitudinal stresses to the external constraints, variations of these stresses during the welding of FS1 and CS1 for a unique node were plotted against time. The node is located on side 1 in the mid-section of the specimen in the welding direction at a distance of 1 mm from the weld toe. As can be seen in Fig. 22(a) and (b), both the transverse and longitudinal stresses become compressive due to expansion of the regions experienced a high temperature of 900 °C. As these areas start to cool down, residual stresses start to rise. The stresses are remarkable for longitudinal stresses

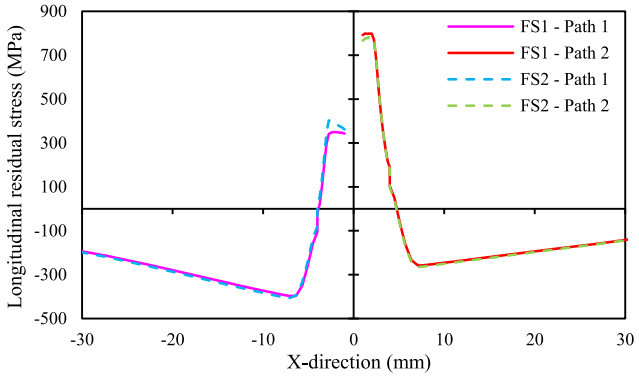

Fig. 20. Simulated longitudinal stresses (S22) for FS1 and FS2 along path 1 and path 2.

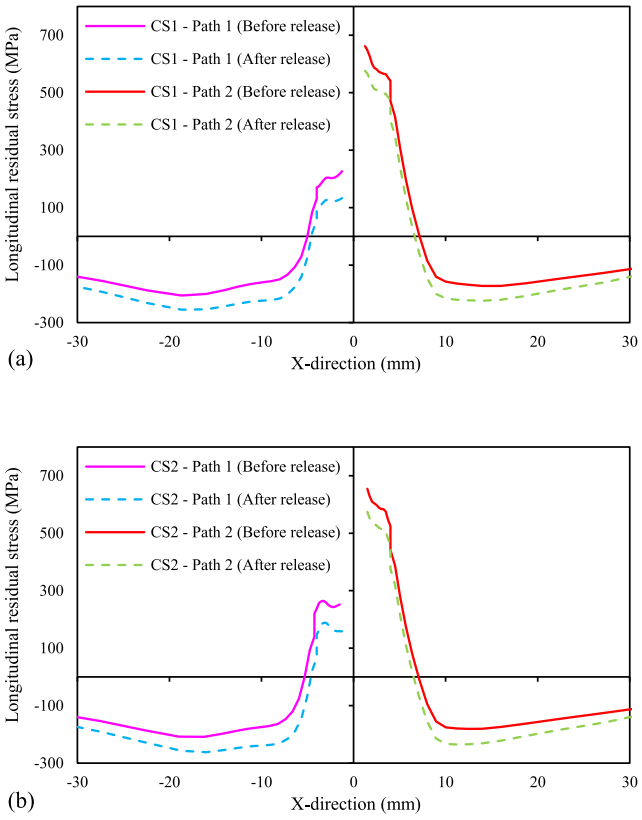

Fig. 21. The simulated longitudinal stresses (S22) along path 1 and path 2 before and after release for: (a) CS1; and (b) CS2.

and remain constant as the specimens reach the ambient temperature. When the second welding pass starts, the stresses become modified, redistributed, and start to fall as the heat reaches these areas. When the second welding pass ends and the specimens cool down to room temperature, residual stresses increase and reach constant levels. Regardless of the final magnitude of the residual stresses in the restrained condition, the change in the levels of the transverse and longitudinal stresses after removal of the clamps is interesting. As can be seen in Fig. 22(a), after unclamping of FS1, which was clamped at one end, the change in the transverse and longitudinal stresses is negligible. In Fig. 22(b), for CS1, which was clamped at both ends, when removing the clamps, the transverse residual stress falls dramatically, while a slight decrease is observable in the magnitude of the longitudinal stress. This implies that transverse stress is sensitive to the stiffness of external constraints and it can be released if the stiffness of the constraint decreases [35]. It should be noted that the fall in the magnitude of the transverse residual stress for this constraint configuration after unclamping depends on its distance from the heat source, i.e., the thermal cycles it experiences.

5. Conclusions and future work

Thermo-elastic-plastic FE models were developed in ABAQUS code to simulate welding temperature fields, transverse residual stresses and angular distortions in T-fillet specimens made from a HSS for two different welding sequences and two mechanical boundary conditions. Supportive measurements in terms of welding temperatures, residual stresses and welding deformations were carried out to verify the developed computational approach. Based on the simulation and the experimental results, the following conclusions are drawn.

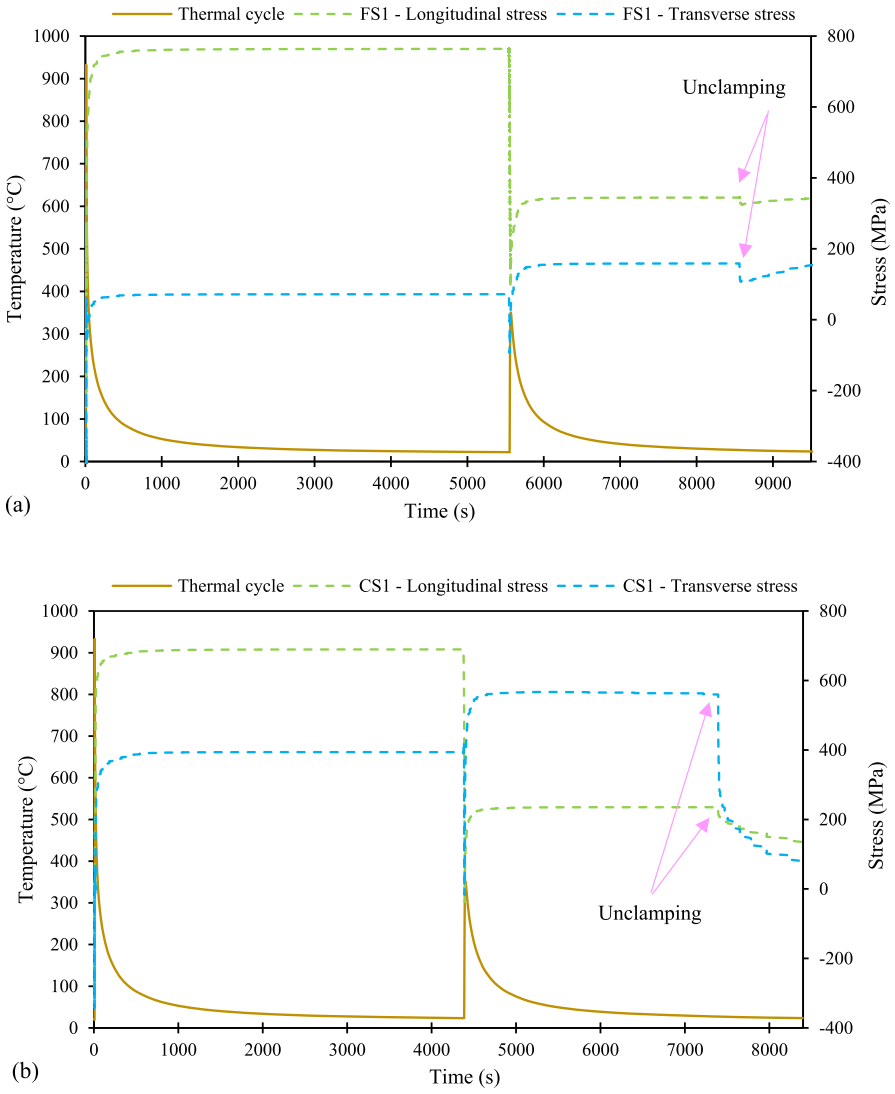

Fig. 22. Evolution of the transverse and longitudinal stresses for a node at a distance of 1 mm from the weld toe during the welding of: (a) FS1; and (b) CS1.

(1) The results of the thermal and mechanical analyses are in good agreement with the experimental measurements. Consequently, it can be concluded that the developed numerical approach can accurately capture distributions of welding angular distortion and residual stresses.
(2) The configuration of mechanical boundary conditions has larger effects on the development of angular distortion and transverse residual stress than welding sequence.
(3) The welding sequence in which the two passes are in the same direction results in less angular distortion and lower peak transverse residual stress than the welding sequence where the welding passes are in the opposite directions. The difference between the peak longitudinal stresses in both the tensile and compressive modes, which developed due to a change in the welding sequence, is minor.
(4) Transverse residual stresses are sensitive to the stiffness degree of the constraints, i.e., a higher degree of restraint can cause an increase in the transverse residual stresses. By removing or reducing the restraining stiffness, transverse stresses can be released or eased. Longitudinal residual stresses are less sensitive to the restraining stiffness of the external constraints.
(5) Using rigid clamping at both ends during the welding and its removal post welding can significantly reduce the angular distortion and lower the levels of the induced residual stresses, especially transverse stresses.
(6) Non-continuous fillet welds are common in practical applications either temporarily (as tack welds) or permanently (as intermittent fillet welds). It is thus of interest to investigate the effect of external constraints and welding sequence on the development of welding angular distortions and residual stresses in non-continuously fillet welded joints made of HSSs.

Declaration of Competing Interest

Hereby, authors of this paper declare no conflict of interest.

Acknowledgements

This research was funded by Business Finland (formerly TEKES) in the DigRob research project. The support of SSAB Europe is acknowledged.

Appendix A. Residual stress components

For structural integrity assessment purposes, the distribution of residual stresses can be discussed based on certain invariant characteristics. Once a through thickness distribution of the residual stress is available, based on the results of an FE model, for example, it can be decomposed into three parts, namely, membrane, bending and self-equilibrating components, which are described by Eqs. (A.1), (A.2), and (A.3), respectively:

$$\sigma_{res,m} = \frac{1}{t}\int_0^t \sigma_{res,x}(z)dz \tag{A.1}$$

$$\sigma_{res,b} = \frac{6}{t^2}\int_0^t \left[\sigma_{res,x}(z) - \sigma_{res,m}\right]\left(\frac{t}{2} - z\right)\mathrm{d}z \tag{A.2}$$

$$\sigma_{res,se} = \sigma_{res,x} - \sigma_{res,m} - \sigma_{res,b}\left(1 - \frac{2z}{t}\right) \tag{A.3}$$

where $\sigma_{res,\ m}$, $\sigma_{res,\ b}$, and $\sigma_{res,\ se}$ are membrane, bending and self-equilibrating components, respectively. t is material thickness and $\sigma_{res,\ x}(z)$ is the transverse residual stress (S11 in this study), which was read from the FE model in the *Z*-direction (through thickness). By applying this decomposition technique for CS1 on side 1 at the weld toe and performing integration over the weld length (by intervals of approximately 3 mm), where $z = 0$ is on the top surface and $z = t$ is on the bottom surface, the following results for the membrane and bending components are observed regarding the clamped and unclamped conditions for the specimen CS1.

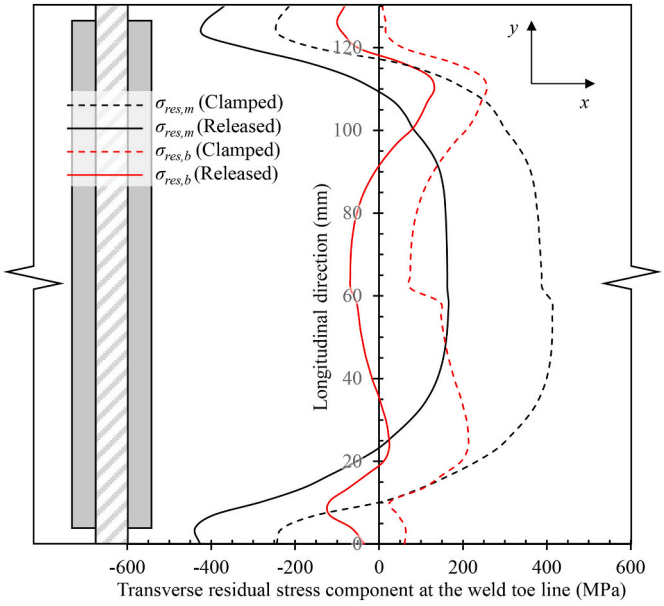

Fig. A.1. Membrane and bending components calculated for CS1 on side 1 at the weld toe in the clamped and released conditions.

As can be seen in Fig. A.1, when the specimen is clamped, the bending and normal components of the residual stresses are considerable and have magnitudes of +238 and +136 MPa calculated based on Eqs. (A.1) and (A.2), respectively. When removing the external constraints, the membrane and bending components reduce in magnitude and tend to reach a zero level and get the magnitudes of −7 and −17 MPa. After unclamping, the residual stresses are self-balanced, although, unequally distributed in the welding direction. It should be noted that the through-thickness residual stresses were not measured, for example by neutron diffraction method, to validate the stress components. However, the distribution of the membrane residual stress component is similar to the conventionally accepted distribution presented in [36]. The stress decomposition technique presented in this section, which uses the results of the FE welding simulation, is applicable to assessment of the stability of plate components and study of the behavior of crack growth under the influence of an unequal residual stress field, and it can help to estimate the stress intensity factor due to residual stresses [37,38].

References

[1] J. Sun, X. Liu, Y. Tong, D. Deng, A comparative study on welding temperature fields, residual stress distributions and deformations induced by laser beam welding and CO2 gas arc welding, Mater. Des. 63 (2014) 519–530, https://doi.org/10.1016/j.matdes.2014.06.057.

[2] D. Deng, Y. Zhou, T. Bi, X. Liu, Experimental and numerical investigations of welding distortion induced by CO2 gas arc welding in thin-plate bead-on joints, Mater. Des. 52 (2013) 720–729, https://doi.org/10.1016/j.matdes.2013.06.013.

[3] C.H. Lee, K.H. Chang, Finite element simulation of the residual stresses in high strength carbon steel butt weld incorporating solid-state phase transformation, Comput. Mater. Sci. 46 (2009) 1014–1022, https://doi.org/10.1016/j.commatsci.2009.05.007.

[4] Z. Barsoum, I. Barsoum, Residual stress effects on fatigue life of welded structures using LEFM, Eng. Fail. Anal. 16 (2009) 449–467, https://doi.org/10.1016/j.engfailanal.2008.06.017.

[5] D. Deng, FEM prediction of welding residual stress and distortion in carbon steel considering phase transformation effects, Mater. Des. 30 (2009) 359–366, https://doi.org/10.1016/j.matdes.2008.04.052.

[6] H. Moshayedi, I. Sattari-Far, The effect of welding residual stresses on brittle fracture in an internal surface cracked pipe, Int. J. Press. Vessel. Pip. 126 (2015) 29–36, https://doi.org/10.1016/j.ijpvp.2015.01.003.
[7] C. Heinze, C. Schwenk, M. Rethmeier, Numerical calculation of residual stress development of multi-pass gas metal arc welding, J. Constr. Steel Res. 72 (2012) 12–19, https://doi.org/10.1016/j.jcsr.2011.08.011.
[8] X.F. Yan, C. Yang, Experimental research and analysis on residual stress distribution of circular steel tubes with different processing techniques, Thin-Walled Struct. 144 (2019) 106268, https://doi.org/10.1016/J.TWS.2019.106268.
[9] T. Skriko, M. Ghafouri, T. Björk, Fatigue strength of TIG-dressed ultra-high-strength steel fillet weld joints at high stress ratio, Int. J. Fatigue 94 (2017) 110–120, https://doi.org/10.1016/j.ijfatigue.2016.09.018.
[10] M. Amraei, A. Ahola, S. Afkhami, T. Björk, A. Heidarpour, X.L. Zhao, Effects of heat input on the mechanical properties of butt-welded high and ultra-high strength steels, Eng. Struct. 198 (2019) 109460, https://doi.org/10.1016/j.engstruct.2019.109460.
[11] T. Björk, A. Ahola, N. Tuominen, On the design of fillet welds made of ultra-high-strength steel, Weld. World 62 (2018) 985–995, https://doi.org/10.1007/S40194-018-0624-4.
[12] J. Ahn, E. He, L. Chen, T. Pirling, J.P. Dear, C.M. Davies, Determination of residual stresses in fibre laser welded AA2024-T3 T-joints by numerical simulation and neutron diffraction, Mater. Sci. Eng. A 712 (2018) 685–703, https://doi.org/10.1016/j.msea.2017.12.027.
[13] M. Rikken, R. Pijpers, H. Slot, J. Maljaars, A combined experimental and numerical examination of welding residual stresses, J. Mater. Process. Technol. 261 (2018) 98–106, https://doi.org/10.1016/j.jmatprotec.2018.06.004.
[14] Y. Danis, E. Lacoste, C. Arvieu, Numerical modeling of inconel 738LC deposition welding: Prediction of residual stress induced cracking, J. Mater. Process. Technol. 210 (2010) 2053–2061, https://doi.org/10.1016/j.jmatprotec.2010.07.027.
[15] B.Q. Chen, C. Guedes Soares, Experimental and numerical investigation on welding simulation of long stiffened steel plate specimen, Mar. Struct. 75 (2021) 102824, https://doi.org/10.1016/J.MARSTRUC.2020.102824.
[16] A. Evdokimov, N. Doynov, R. Ossenbrink, A. Obrosov, S. Weiß, V. Michailov, Thermomechanical laser welding simulation of dissimilar steel-aluminum overlap joints, Int. J. Mech. Sci. 190 (2021) 106019, https://doi.org/10.1016/J.IJMECSCI.2020.106019.
[17] C. Chen, S.P. Chiew, M.S. Zhao, C.K. Lee, T.C. Fung, Influence of cooling rate on tensile behaviour of S690Q high strength steel butt joint, J. Constr. Steel Res. 173 (2020) 106258, https://doi.org/10.1016/J.JCSR.2020.106258.
[18] A.A. Bhatti, Z. Barsoum, H. Murakawa, I. Barsoum, Influence of thermo-mechanical material properties of different steel grades on welding residual stresses and angular distortion, Mater. Des. 65 (2015) 878–889, https://doi.org/10.1016/j.matdes.2014.10.019.
[19] X. Hu, G. Feng, Y. Wang, C. Zhang, D. Deng, Influence of lumping passes on calculation accuracy and efficiency of welding residual stress of thick-plate butt joint in boiling water reactor, Eng. Struct. 222 (2020) 111136, https://doi.org/10.1016/j.engstruct.2020.111136.
[20] P. Dai, Y. Wang, S. Li, S. Lu, G. Feng, D. Deng, FEM analysis of residual stress induced by repair welding in SUS304 stainless steel pipe butt-welded joint, J. Manuf. Process. 58 (2020) 975–983, https://doi.org/10.1016/j.jmapro.2020.09.006.
[21] M. Ghafouri, J. Ahn, J. Mourujärvi, T. Björk, J. Larkiola, Finite element simulation of welding distortions in ultra-high strength steel S960 MC including comprehensive thermal and solid-state phase transformation models, Eng. Struct. 219 (2020) 110804, https://doi.org/10.1016/j.engstruct.2020.110804.
[22] Q. Zhang, Y. Ma, C. Cui, X. Chai, S. Han, Experimental investigation and numerical simulation on welding residual stress of innovative double-side welded rib-to-deck joints of orthotropic steel decks, J. Constr. Steel Res. 179 (2021) 106544, https://doi.org/10.1016/J.JCSR.2021.106544.
[23] M. Kubiak, W. Piekarska, Comprehensive model of thermal phenomena and phase transformations in laser welding process, Comput. Struct. 172 (2016) 29–39, https://doi.org/10.1016/j.compstruc.2016.05.014.
[24] Z. Barsoum, A. Lundbäck, Simplified FE welding simulation of fillet welds - 3D effects on the formation residual stresses, Eng. Fail. Anal. 16 (2009) 2281–2289, https://doi.org/10.1016/j.engfailanal.2009.03.018.
[25] W. Liang, X. Hu, Y. Zheng, D. Deng, Determining inherent deformations of HSLA steel T-joint under structural constraint by means of thermal elastic plastic FEM, Thin-Walled Struct. 147 (2020) 106568, https://doi.org/10.1016/j.tws.2019.106568.
[26] ABAQUS user's manual, Version 2020, 2020.
[27] J. Goldak, A. Chakravarti, M. Bibby, A new finite element model for welding heat sources, Metall. Trans. B 15 (1984) 299–305, https://doi.org/10.1007/BF02667333.
[28] J. Siltanen, S. Tihinen, J. Kömi, Laser and laser gas-metal-arc hybrid welding of 960 MPa direct-quenched structural steel in a butt joint configuration, J. Laser Appl. 27 (2015), S29007, https://doi.org/10.2351/1.4906386.
[29] D. Deng, H. Murakawa, W. Liang, Numerical simulation of welding distortion in large structures, Comput. Methods Appl. Mech. Eng. 196 (2007) 4613–4627, https://doi.org/10.1016/J.CMA.2007.05.023.
[30] D. Deng, H. Murakawa, Numerical simulation of temperature field and residual stress in multi-pass welds in stainless steel pipe and comparison with experimental measurements, Comput. Mater. Sci. 37 (2006) 269–277, https://doi.org/10.1016/J.COMMATSCI.2005.07.007.
[31] C.H. Lee, K.H. Chang, Prediction of residual stresses in high strength carbon steel pipe weld considering solid-state phase transformation effects, Comput. Struct. 89 (2011) 256–265, https://doi.org/10.1016/j.compstruc.2010.10.005.
[32] A. Yaghi, T.H. Hyde, A.A. Becker, W. Sun, J.A. Williams, Residual stress simulation in thin and thick-walled stainless steel pipe welds including pipe diameter effects, Int. J. Press. Vessel. Pip. 83 (2006) 864–874, https://doi.org/10.1016/j.ijpvp.2006.08.014.
[33] B. Brickstad, B.L. Josefson, A parametric study of residual stresses in multi-pass butt-welded stainless steel pipes, Int. J. Press. Vessel. Pip. 75 (1998) 11–25, https://doi.org/10.1016/S0308-0161(97)00117-8.
[34] K. Seleš, M. Perić, Z. Tonković, Numerical simulation of a welding process using a prescribed temperature approach, J. Constr. Steel Res. 145 (2018) 49–57, https://doi.org/10.1016/J.JCSR.2018.02.012.
[35] G. Fu, M.I. Lourenco, M. Duan, S.F. Estefen, Effect of boundary conditions on residual stress and distortion in T-joint welds, J. Constr. Steel Res. 102 (2014) 121–135, https://doi.org/10.1016/J.JCSR.2014.07.008.
[36] K. Masubuchi, Analysis of Welded Structures: Residual Stresses, Distortion, and their Consequences, Pergamon Press, 1980.
[37] S. Bhardwaj, R.M. Chandima Ratnayake, Residual stress estimation in defect assessment procedures at weld toe and away locations on girth welds: Review of key parameters, Theor. Appl. Fract. Mech. 111 (2021) 102848, https://doi.org/10.1016/J.TAFMEC.2020.102848.
[38] P. Dong, Length scale of secondary stresses in fracture and fatigue, Int. J. Press. Vessel. Pip. 85 (2008) 128–143, https://doi.org/10.1016/J.IJPVP.2007.10.005.